Optical coherence tomography image denoising using Gaussianization transform

Zahra Amini
Hossein Rabbani

Optical coherence tomography image denoising using Gaussianization transform

Zahra Amini and Hossein Rabbani*
Isfahan University of Medical Sciences, School of Advanced Technologies in Medicine, Medical Image and Signal Processing Research Center, Department of Biomedical Engineering, Isfahan, Iran

Abstract. We demonstrate the power of the Gaussianization transform (GT) for modeling image content by applying GT for optical coherence tomography (OCT) denoising. The proposed method is a developed version of the spatially constrained Gaussian mixture model (SC-GMM) method, which assumes that each cluster of similar patches in an image has a Gaussian distribution. SC-GMM tries to find some clusters of similar patches in the image using a spatially constrained patch clustering and then denoise each cluster by the Wiener filter. Although in this method GMM distribution is assumed for the noisy image, holding this assumption on a dataset is not investigated. We illustrate that making a Gaussian assumption on a noisy dataset has a significant effect on denoising results. For this purpose, a suitable distribution for OCT images is first obtained and then GT is employed to map this original distribution of OCT images to a GMM distribution. Then, this Gaussianized image is used as the input of the SC-GMM algorithm. This method, which is a combination of GT and SC-GMM, remarkably improves the results of OCT denoising compared with earlier version of SC-GMM and even produces better visual and numerical results than the state-of-the art works in this field. Indeed, the main advantage of the proposed OCT despeckling method is texture preservation, which is important for main image processing tasks like OCT inter- and intraretinal layer analysis. Thus, to prove the efficacy of the proposed method for this analysis, an improvement in the segmentation of intraretinal layers using the proposed method as a preprocessing step is investigated. Furthermore, the proposed method can achieve the best expert ranking between other contending methods, and the results show the helpfulness and usefulness of the proposed method in clinical applications.
© 2017 Society of Photo-Optical Instrumentation Engineers (SPIE) [DOI: 10.1117/1.JBO.22.8.086011]

Keywords: optical coherence tomography images; denoising, spatially constrained Gaussian mixture model; Gaussianization transform.

Paper 170141RR received Mar. 3, 2017; accepted for publication Aug. 1, 2017; published online Aug. 29, 2017.

1 Introduction

Optical coherence tomography (OCT) is a recently created imaging technique to illustrate different information about the internal structures of an object. As in ultrasound imaging, OCT is based on interferometric techniques, except that OCT uses light beams instead of sound profiles.[1] Use of OCT images is more popular in the field of ophthalmology, where it has become a key diagnostic technology in the areas of retinal diseases.[2] OCT images usually suffer from speckle noise, which restricts the ability of image interpretation. Hence, noise reduction techniques are an essential process for these images. In a wide division, OCT denoising methods can be classified into two basic groups: methods that reduce the noise by some modifications on OCT device imaging such as Refs. 3 and 4 (based on hardware) and the methods that work on the recorded data (based on software). Because of our limitation in access to hardware of devices, we focus more on the second group of denoising methods. Based on our categorization in Ref. 5, these methods can be applied on the spatial or transform domain. For reducing noise in OCT images in the spatial domain, usually some simple methods like low-pass filters, linear smoothing, mean, median, and Wiener filters are used. However, some developed methods like multiple uncorrelated

B-scan averaging,[6,7] nonlinear anisotropic filter,[8,9] complex diffusion,[10,11] directional filtering,[12,13] adaptive vector-valued kernel function,[14] support vector machine approach,[15] and Bayesian estimations[16] are also applied in the spatial domain.

In the transform based group, some data adaptive methods like principle component analysis;[17] dictionary learning;[18,19] some nondata adaptive methods that are based on wavelets,[20,21] dual-tree complex wavelet transform[22,23] or curvelets;[24,25] and a circular symmetric Laplacian mixture model in wavelet diffusion[26] have been applied for denoising.

Recently, some groups of investigators[27] improved the result of denoising by combining dictionary learning and wavelet thresholding and by defining a proper data-dependent initial dictionary.

In another point of view, the denoising problem may be solved in a deterministic or statistical framework.[23] In the first framework, each pixel is considered an unknown deterministic variable, and non-Bayesian techniques are used for denoising. In the statistical framework, a random field is employed to model the data, and Bayesian methods are applied to estimate noise-free data. Thus, finding a suitable prior probability distribution function (pdf) for noise-free data plays an important role in the denoising problem.[23] Although there is a large body of work on OCT image analysis, few studies have been done on

---

*Address all correspondence to: Hossein Rabbani, E-mail: rabbani.h@ieee.org

OCT images from a statistical modeling point of view. One of these studies is the work of Grzywacz et al.[28] in which a probability model for OCT data was suggested and used for early detection of diabetic retinopathy. The denoising method that is proposed in this paper is the second type (statistical framework), so it first needs to obtain an appropriate statistical model for OCT images.

Another issue is that assumption of the Gaussianity plays a key role in many signal processing methods. For example, a Wiener filter is a linear minimum-mean-square error filter in which the observed and noise-free data are jointly Gaussian. It is proven that, for a Gaussian process, nonlinear filters do not lead to better results compared with a Wiener filter. However, sometimes researchers use this Wiener filtering method without considering this Gaussianity assumption, so they cannot fully benefit from the ability of the algorithm. In this paper, it is illustrated that holding this assumption has a notable effect on the denoising results. Therefore, in this work, a Gaussianization transform (GT) that maps the original distribution of the OCT data to Gaussian components is introduced, and, with this transform, all of the good characteristics of the Gaussian process can be used.

In the rest of the paper, a powerful patch-based denoising method, namely the spatially constrained Gaussian mixture model (SC-GMM), is first explained in Sec. 2.1. Since SC-GMM is based on the Gaussian distribution assumption of noise-free data, which is not satisfied for OCT images, in Sec. 2.2 GT is applied on OCT data. By applying GT, the distribution of transformed OCT data is expressed by a combination of Gaussian pdfs. In this base, the proposed denoising method, which is a combination of Gaussianization and SC-GMM, is demonstrated in Sec. 2.3. The visual and numerical results of the proposed OCT denoising method are presented in Sec. 3, and Sec. 4 presents the discussion of our results in comparison with the state of the art methods. Finally, a summary of this paper is presented in Sec. 5.

2 Method

Today, patch-based image denoising methods are known as an effective way for denoising natural images.[29–31] The proposed denoising method in this paper is also a patch-based technique; it is a modified version of the SC-GMM algorithm introduced by Niknejad et al.[32] In Sec. 2.1, the SC-GMM method that is based on a Gaussian distribution assumption of similar image patches in a neighborhood is described. However, it is clear that this assumption is not satisfied for all kinds of datasets like OCT images. Thus, after investigation of the distribution of the original OCT image, it is necessary to convert it to a Gaussian distribution for which GT is used. These steps are explained in Sec. 2.2 and finally the proposed OCT denoising method, which is a combination of GT and SC-GMM, is introduced in Sec. 2.3.

2.1 SC-GMM Denoising Method

As mentioned above, SC-GMM denoising is a patch-based method in which the whole of the image is partitioned into overlapping patches and it is assumed that each set of neighbor patches can be modeled using a multivariate Gaussian pdf with a specific mean vector and covariance matrix. For this purpose, some exemplar patches are uniformly chosen from the whole image; then, similar patches in the vicinity of each exemplar patch are grouped together to construct a region using the

K-nearest neighbors (KNN) algorithm. To determine these clusters of patches and estimate the parameters of Gaussian pdfs (covariance matrices and mean vectors), a two-step approach is applied.[33] This estimation approach includes a clustering step and a denoising step.

Assume $y = x + n$ is a noisy image, where x is noise-free data and n is an independent zero-mean Gaussian noise with known variance σ_n^2. Also, let x_r denote the r'th exemplar patch with mean vector μ_r and covariance matrix Σ_r for $r = 1, \ldots, R$. After initialization, $\hat{x} = y$, the following steps are iteratively implemented:

Clustering step. In this step, for each exemplar patch $\hat{x}_r$, KNN patches $\hat{x}_i$, $i = 1, \ldots, K$, that have minimum dissimilarity (based on l_2 norm metric, i.e., $d = \|\hat{x}_r - \hat{x}_i\|_2^2$) with the exemplar patch are chosen. These $\hat{x}_r$ and $\hat{x}_i$s are estimated in the previous iteration or the initialization in the first step.

Denoising step. The goal of this step is to restore the image using the clusters obtained in the clustering step. Thus, first the parameters of Gaussian distribution for each set of patches are estimated using the maximum likelihood method

$$\hat{\mu}_r = \frac{1}{K} \sum_{i \in S_r} \hat{x}_i, \tag{1}$$

$$\hat{\Sigma}_r = \frac{1}{K} \sum_{i \in S_r} (\hat{x}_i - \hat{\mu}_r)(\hat{x}_i - \hat{\mu}_r)^{\mathrm{T}}, \tag{2}$$

where S_r shows the set of KNN patches in the r'th region. It should be noted that in our implementation the above sample covariance matrix is not invertible, so as with similar works,[34] an eigenvalue regularization is applied using

$$\hat{\Sigma}_r = \hat{\Sigma}_r + \delta I, \tag{3}$$

where δ is a small constant (here $\delta = 0.1$) and I is the identity matrix.

After estimating the parameters of the Gaussian pdf, the denoised patch $\hat{x}_i$ in the r'th region is found by maximizing *a posteriori* function $\log p(x|y_i, \hat{\mu}_r, \hat{\Sigma}_r)$, i.e.,

$$\hat{x}_i = \arg \max_x \log p(x|y_i, \hat{\mu}_r, \hat{\Sigma}_r)$$
$$= \arg \min_x \|y_i - x\|_2^2 + \sigma_n^2 (x - \hat{\mu}_r)^{\mathrm{T}} \hat{\Sigma}_r^{-1} (x - \hat{\mu}_r), \tag{4}$$

where y_i is the corresponding noisy observed patch and Eq. (4) is derived from the assumption of the Gaussian pdf for noise-free patch and noise, i.e., $x_i \sim \mathcal{N}(\hat{\mu}_r, \hat{\Sigma}_r)$ and $n \sim \mathcal{N}(0, \sigma_n^2 I)$, respectively.

By setting the derivative of Eq. (4) to zero, this optimization problem can be solved, which leads to the linear Wiener filter as follows:

$$\hat{x}_i = (I + \sigma_n^2 \hat{\Sigma}_r^{-1})^{-1}(y_i + \sigma_n^2 \hat{\Sigma}_r^{-1} \hat{\mu}_r). \tag{5}$$

The last step for reconstructing the whole image is averaging the weighted restored patches. In this work, based on Ref. 32, these weights are considered proportional to similarity to Gaussian distributions. To be more explicit, patches that are more likely to be generated from the estimated Gaussian distribution of their allocated clusters benefit from higher weights. Thus, the weight of the patch $\hat{x}_i$ in the r'th region is obtained by

$$w(i, r) = \exp\left[-\frac{\gamma}{2}(\hat{x}_i - \hat{\mu}_r)^T \hat{\Sigma}_r^{-1}(\hat{x}_i - \hat{\mu}_r)\right], \qquad (6)$$

where γ is an appropriate scaling constant.

Using these weights and averaging on all patches, the denoised image is found. Figure 1 shows the block diagram of the SC-GMM method for image denoising.

2.2 Gaussianization as a Preprocessing Step

In fact, the assumption of Gaussianity plays an important role in many signal processing methods. For example, in this work, the Gaussian distribution assumption for a dataset causes the derivation of the Wiener filter as an optimal linear filter for denoising. Thus, the best denoising result is reached when the initial assumption of Gaussianity is satisfied. However in Ref. 32 and other related works,[34] holding this Gaussianity assumption for the pdf of data is not investigated, and here we demonstrate the importance of this assumption by converting the pdf of OCT intraretinal layers to Gaussian distribution and comparing denoising results with and without Gaussianization. For this purpose, the distribution of the OCT images should first be determined, and then an appropriate GT is designed to convert the OCT original distribution to a GMM and satisfy the initial assumption for our denoising algorithm. The block diagram of the Gaussianization process is displayed in Fig. 2.

2.2.1 OCT distribution estimation

Since the speckle noise in the OCT images is a multiplicative noise and working with the additive noise is simpler and more common, first, a logarithm operator is used to convert this noise to an additive Gaussian noise. Thus, all the processes are implemented in the logarithmic domain. In Ref. 35, we discussed that, because of the layered structure of the retina, a mixture model can be well fitted to a whole OCT B-scan.

Moreover, a monotonically decaying behavior of the OCT intensities in each layer means that leptokurtic distributions such as the Laplace pdf are good candidates for describing the statistical properties of layers.[35] On the other hand, this

image is corrupted with the additive white Gaussian noise in the logarithmic space, so an appropriate statistical model for an OCT image is a mixture distribution. Each component of this mixture model is composed of a Laplace random variable x_j, plus a Gaussian noise n. We called this model a normal-Laplace mixture (NLM) model and described it in detail in Ref. 35.

Indeed, for each component of the mixture model, we would have $y_j = x_j + n$, where the pdfs of x_j and n are

$$f_{X_j}(x) = \frac{1}{\sqrt{2}\sigma_j} \exp\left(-\frac{\sqrt{2}}{\sigma_j}|x - \mu_j|\right), \qquad (7)$$

$$f_N(n) = \frac{1}{\sqrt{2\pi}\sigma_n} \exp\left(-\frac{n^2}{2\sigma_n^2}\right). \qquad (8)$$

μ_j shows the mean of the Laplace variable and σ_j and σ_n display the scaling parameters of the Laplace and Gaussian distributions, respectively.

Since $y_j = x_j + n$ and the noise signal n is assumed to be independent from the noise-free signal x_j, the pdf of the normal-Laplace variable y_j is given by the convolution

$$f_j(y) = (f_{X_j} * f_N)(y) = \int_{-\infty}^{+\infty} f_{X_j}(x) f_N(y - x) dx. \qquad (9)$$

After some mathematical computations, we have[35]

$$f_j(y) = \frac{-1}{2\sqrt{2}\sigma_j}\left\{\exp\left[\frac{\sigma_n^2}{\sigma_j^2} + \frac{\sqrt{2}(y-\mu_j)}{\sigma_j}\right]\text{erfc}\left[-\frac{(y-\mu_j)}{\sqrt{2}\sigma_n} - \frac{\sigma_n}{\sigma_j}\right]\right.$$
$$\left. - \exp\left[\frac{\sigma_n^2}{\sigma_j^2} - \frac{\sqrt{2}(y-\mu_j)}{\sigma_j}\right]\text{erfc}\left[-\frac{(y-\mu_j)}{\sqrt{2}\sigma_n} + \frac{\sigma_n}{\sigma_j}\right]\right\},$$
$$(10)$$

where $\text{erfc}(x) = e^{-x^2}\text{erfc}\,x(x) = \frac{2}{\sqrt{\pi}}\int_0^\infty e^{-x^2-t^2-2tx}dt$.
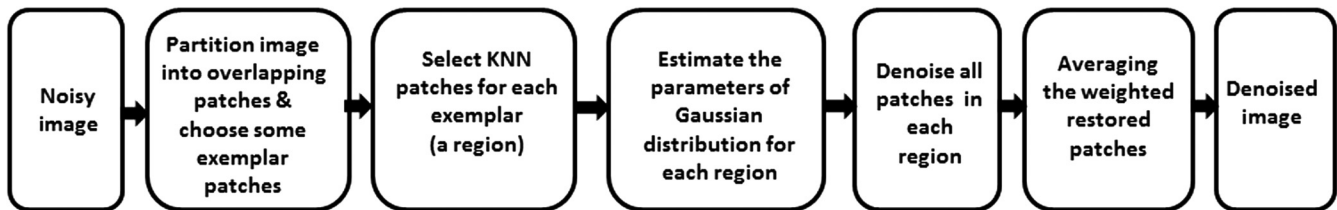

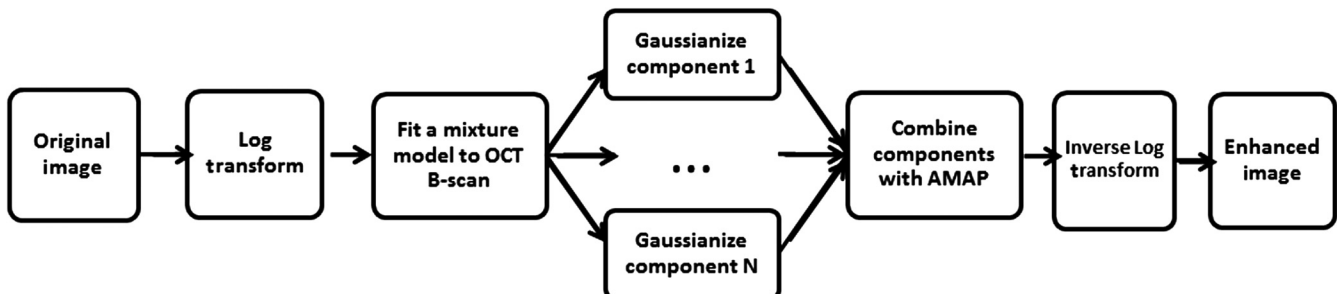**Fig. 1** Block diagram of spatially constrained GMM (SC-GMM) method for image denoising.

Fig. 2 Block diagram of GT.

Thus, y_j has a normal-Laplace distribution, and we show it by $y_j \sim NL(\mu_j, \sigma_j, \sigma_n)$. Additionally, the pdf of the NLM model is presented by $g_Y(y)$ as follows:

$$g_Y(y) = \sum_{j=1}^{J} a_j f_j(y), \tag{11}$$

where $f_j(y)$ is the pdf of each component, $a_j \geq 0$, $\sum_{j=1}^{J} a_j = 1$, and J is the number of mixture components. In Ref. 35, it has been shown that the choice of $J = 5$ causes the best results.

After finding a proper model, its parameters are estimated based on a used dataset. The EM algorithm[36] is used to estimate parameters iteratively as follows:

- E-step: In each iteration, the responsibility factors r_j (as an auxiliary variable that for each observed data y represents how likely that observed data was produced by each component $\{f_j(y)\}_{j=1:J}$) are updated by

$$r_j \leftarrow \frac{a_j f_j(y)}{\sum_{j=1}^{J} a_j f_j(y)}, \quad \text{for } j = 1, \ldots, J. \tag{12}$$

- M-step: Then, the parameters a_j are updated by

$$a_j \leftarrow \sum_{l=1}^{N} r_j(l)/N, \tag{13}$$

where N shows the number of pixels in image y.

In the M-step, the updated equations for $\{\mu_j, \sigma_j\}_{j=1}^{J}$ are approximately estimated as[37]

$$\mu_j \leftarrow \sum_{l=1}^{N} y. \, r_j(l)/ \sum_{l=1}^{N} r_j(l), \tag{14}$$

$$\sigma_j^2 \leftarrow \max \left\{ \sum_{l=1}^{N} |y - \mu_j|^2 r_j(l) / \sum_{l=1}^{N} r_j(l), \delta \right\}, \tag{15}$$

where δ is a small positive constant number used to avoid numerical errors.

2.2.2 Gaussianization transform

As mentioned before, SC-GMM has been designed based on Gaussianity assumption. However, the distribution of each OCT intraretinal layer can be modeled as a normal-Laplace pdf.[35] Thus, if a GT is designed to map the original distribution to a Gaussian distribution, it is expected to obtain better denoising results. The core of this transform is solving the equation that compares the cumulative distribution function (CDF) of original dataset and Gaussian distribution. Assume $F_W(w) = 0.5[1 + \text{erf}(\frac{w - \mu_w}{\sqrt{2}\sigma_w})]$ expresses the CDF of a Gaussian variable (w) with μ_w and σ_w as the mean and standard deviation of w, respectively, and $\text{erf}(x) = \frac{2}{\sqrt{\pi}} \int_0^x e^{-t^2} dt$. Also, by computing the integral of $f_j(y)$ in Eq. (10), the CDF of a normal-Laplace variable is found as

$$F_j(y) = \frac{1}{2} \left\{ 1 + \text{erf} \left[\frac{(y - \mu_j)}{\sqrt{2}\sigma_n} \right] - \exp \left[\frac{\sigma_n^2}{\sigma_j^2} + \frac{-\sqrt{2}(y - \mu_j)}{\sigma_i} \right] \right. $$
$$+ \frac{1}{2} e^{-\left[\frac{(y-\mu_j)}{\sqrt{2}\sigma_n} \right]^2} \left\{ \text{erfc} \, x \left[\frac{(y - \mu_j)}{\sqrt{2}\sigma_n} + \frac{\sigma_n}{\sigma_j} \right] \right.$$
$$\left. \left. + \text{erfc} \, x \left[\frac{(y - \mu_j)}{\sqrt{2}\sigma_n} - \frac{\sigma_n}{\sigma_j} \right] \right\} \right\}. \tag{16}$$

By equating these two CDFs, one can find an equation that expresses each value of variable y in the initial distribution, in terms of the equivalent value of w in Gaussian space

$$F_Y(y) = F_W(w) \Rightarrow w = \mu_w + \sqrt{2}\sigma_w . \text{erfinv}[2F_Y(y) - 1], \tag{17}$$

where erfinv is the inverse of the error function.

2.2.3 Construct a GMM distribution

After Gaussianization, the distribution of each component of the NLM model, w_j, $j = 1, \ldots, J$, becomes Gaussian; by combining these Gaussian components, an image with the GMM pdf is constructed and can be used as the input of the SC-GMM denoising method. In Ref. 38, it is shown that the averaged maximum *a posterior* (AMAP) method is a suitable way for defining the weights of summation for mixture models. In this method, the weight of each component is defined as $a_j f_j(y)/\sum_{j=1}^{J} a_j f_j(y)$, so $\hat{y}$, as the Gaussianized image with GMM distribution, is obtained as follows:

$$\hat{y} = \sum_{j=1}^{J} a_j . w_j . f_j(y) / \sum_{j=1}^{J} a_j f_j(y). \tag{18}$$

Also, in Ref. 39, it was discussed that instead of using the univariate weighting function $a_j f_j(y)/\sum_{j=1}^{J} a_j f_j(y)$, employing multivariate weighting function leads to better results. Thus, for an OCT image of size $S \times T$, a local $P \times Q$ window (where P and Q are odd) is placed around each pixel $y_{s,t}$ for $s = 1, \ldots, S$, $t = 1, \ldots, T$; and the multivariate function $\bar{f}_j(y)$ for the central pixel of window $(y_{p,q})$ is calculated by multiplying all univariate $f_j(y)s$ in that window i.e.
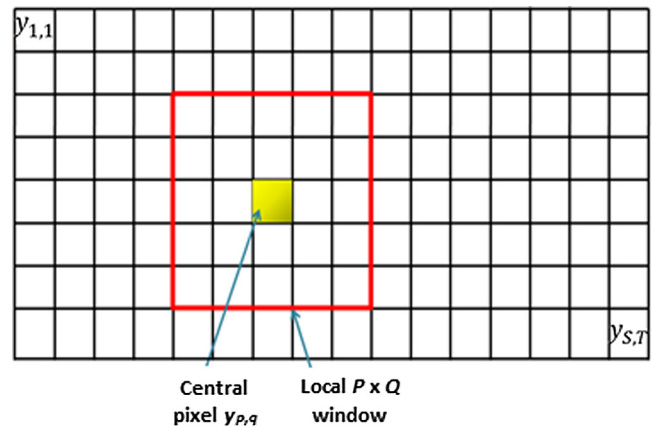

Fig. 3 Using local window around pixels to make a multivariate weighting function $\bar{f}_j(y)$.

$$\bar{f}_j(y_{p,q}) = \prod_{k=-\frac{P-1}{2}}^{\frac{P-1}{2}} \prod_{l=-\frac{Q-1}{2}}^{\frac{Q-1}{2}} f_j(y_{p+k,q+l}). \qquad (19)$$

Figure 3 shows how the multivariate function $\bar{f}_j(y)$ is produced.

Hence, Eq. (18) is replaced with

$$\hat{y} = \frac{\sum_{j=1}^{J} a_j . w_j . \bar{f}_j(y)}{\sum_{j=1}^{J} a_j \bar{f}_j(y)}. \qquad (20)$$

2.3 Proposed Denoising Method

According to Secs. 2.2.1 and 2.2.2, our proposed OCT denoising method is obtained by combining GT and the SC-GMM method as shown in Fig. 4. In this method, the OCT image in the log domain is first Gaussianized using the block diagram of Fig. 2, and then the Gaussianized image is denoised by the SC-GMM method using the block diagram of Fig. 1.

The proposed denoising algorithm can be summarized in the following steps:

1. Transform image to the logarithmic domain

2. Fit an NLM model to the data using the EM algorithm:

   2.1 Initialization: choose initial values for a_j, μ_j, σ_j
   2.2 E-step: compute responsibility factors using Eq. (12)
   2.3 M-step: update parameters a_j, μ_j, σ_j using Eqs. (13)–(15)
   2.4 Iteration: substitute the updated parameters in the previous step for calculating $f_j(y)$

3. Calculate the CDF of each normal-Laplace component by substituting final values of μ_j, σ_j, and σ_n in Eq. (16)

4. Gaussianize each normal-Laplace component using Eq. (17)

5. Use AMAP method in Eq. (20) to obtain the image $\hat{y}$ with GMM distribution

6. Apply SC-GMM algorithm on image $\hat{y}$:

   6.1 Partition image into overlapping patches and choose exemplar patches
   6.2 For each exemplar patch:

      6.2.1 Select KNN patches (a region) based on l_2 norm metric in a finite sized window around exemplar patch
      6.2.2 Estimate Gaussian parameters in each region by Eqs. (1)–(3)
      6.2.3 Denoise the patches in each region by the Wiener filter Eq. (5)

   6.3. Obtain reconstructed image by weighted average of denoised patches using Eq. (6)

7. Apply exponential operator to find the denoised image.

3 Results

In this section, some simulation results performed on our dataset are presented. This dataset consists of thirteen three-dimensional (3-D) macular spectral domain OCT images obtained from eyes without pathologies using a Topcon 3DOCT-1000 imaging system in the Ophthalmology Department of Feiz Hospital, Isfahan, Iran. The x, y, z size of the obtained volumes was $512 \times 650 \times 128$ voxels, $7 \times 3.125 \times 3.125$ mm^3, voxel size $13.67 \times 4.81 \times 24.41$ μm^3.

From this dataset, 130 B-scans were selected randomly (10 B-scans from each subject), and these randomly selected B-scans were denoised with the methods described previously in the paper: once images were denoised only using the SC-GMM method and they were then despeckled by a combination of GT and the SC-GMM according to our method.

Considering the constant values and parameters, for each region, $K = 40$ nearest neighbor patches were accumulated. The exemplar patches were selected every 10 pixels along both the column and row directions of the image. The size of the constraining window around each exemplar patch was set to 30×30, and the size of patches was selected as 10×10. Also, the size of local window around each pixel for obtaining multivariate $\bar{f}_j(y)$ was 3×3. All of these values were selected based on previous related work and our implementation experiences.

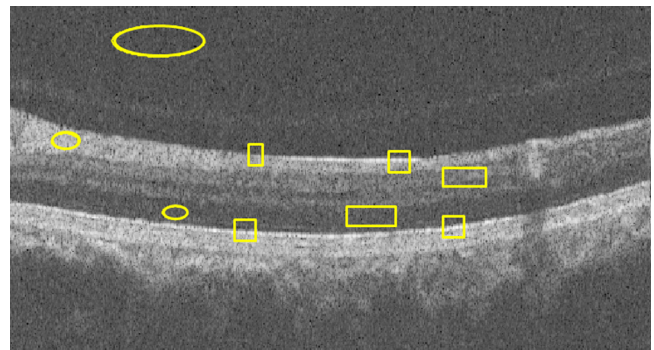Both the qualitative and quantitative performance of the proposed combined method and SC-GMM were provided. The

Fig. 5 Selected ROIs for calculation of CNR, EP, and TP. The larger elliptical region outside the retinal layers is used as background ROI and other circles represent foreground ROIs for CNR calculation. Rectangular ROIs are used for TP and EP.
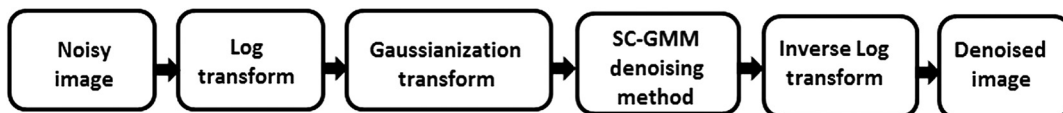

Fig. 4 Block diagram of the proposed combined denoising method, in this figure, third block "GT" includes all the blocks in Fig. 2 (except the Log block) and fourth block "SC-GMM denoising method" is equivalent to the block diagram of Fig. 1.

results of denoising with a simple Wiener filter was also prepared to compare with the proposed approach and prove the need and benefit of GT in the proposed method. Contrast to noise ratio (CNR), edge preservation (EP), and texture preservation (TP) as quantitative measures were computed for each denoising method. The mentioned values were computed based on methods discussed in Ref. 40, and regions for analysis of each criterion are shown in Fig. 5.

CNR measures the contrast between a feature of interest and background noise. EP computes the correlation between edges in the denoised image and the noisy image over the locally selected region of interest (ROI). TP shows the degree of preserving texture in an ROI. Both the TP and EP measures range between 0 and 1 and, in the best condition, go to 1.

In addition, to illustrate the power of the proposed method, its ability in OCT denoising was compared with the BM3D as a benchmark denoising algorithm and recently reported state-of-the-art algorithm in this field.[27] Kafieh et al.[27] proposed a strong method in speckle reduction of OCT datasets in two-dimensional and 3-D by the combination of dictionary learning and wavelet thresholding. They improved the performance of simple dual-tree complex wavelets by taking advantage of adaptability in dictionary learning methods and introducing complex wavelet-based K-SVD. They also compared their algorithm by other previous outstanding researches in this filed like Fang et al.,[18] Yang et al.,[41] and Luan and Wu[17] and demonstrated the superiority of their method. Thus, this complex wavelet-based K-SVD method (3DCWT-KSVD)[27] is chosen as a proper reference
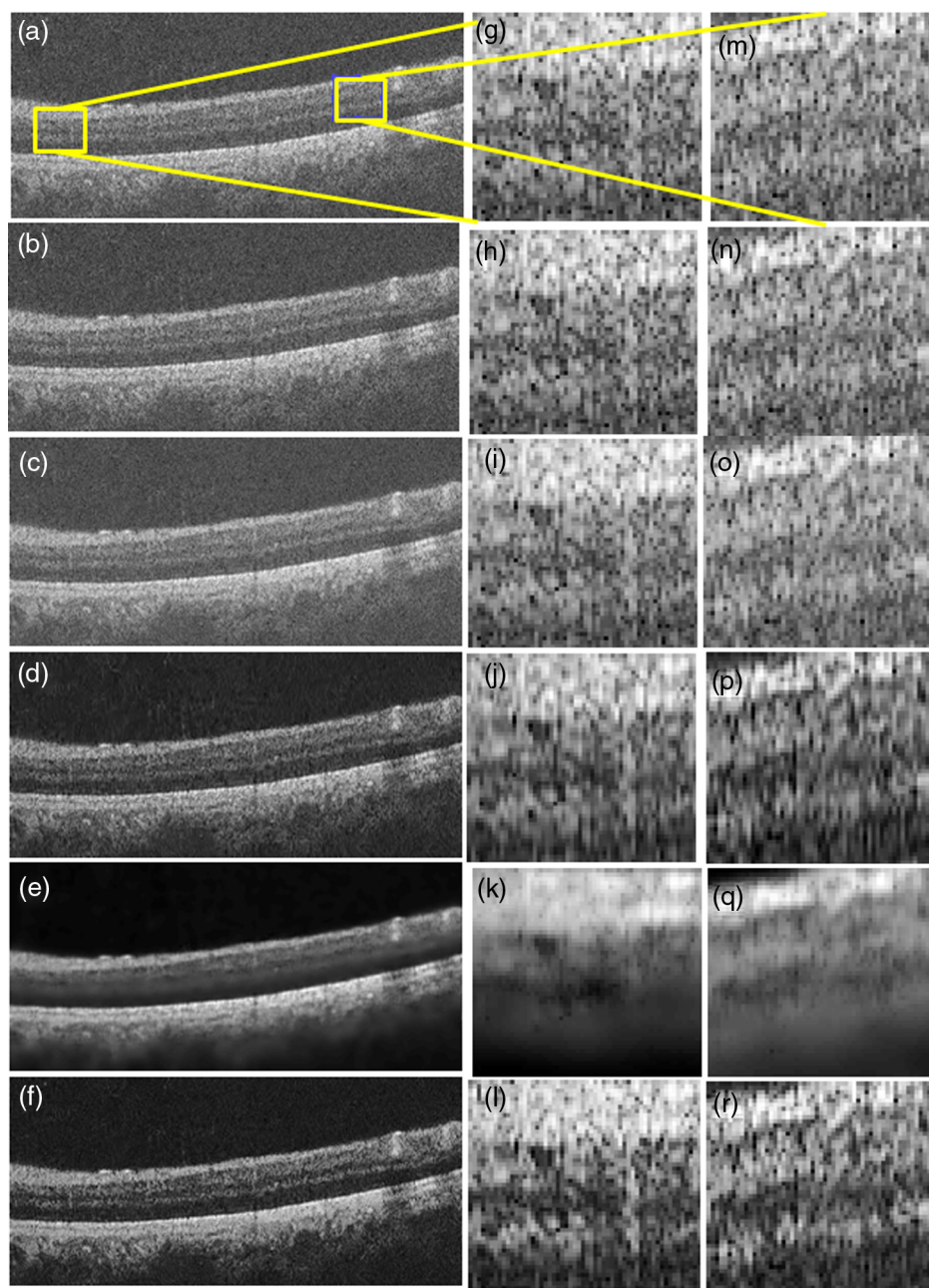

Fig. 6 Denoising results in a sample B-scan. The second and third columns show an enlargement of the specified regions of first column images. (a), (g), (m) Original noisy image; (b), (h), (n) simple Wiener; (c), (i), (o) SC-GMM; (d), (j), (p) BM3D; (e), (k), (q) 3DCWT-KSVD; (f), (l), (r) proposed method.

to evaluate our proposed method. Figures 6 and 7 show some samples of datasets after application of each one of the mentioned denoising methods (simple Wiener, SC-GMM, 3DCWT-KSVD, BM3D, and the proposed method). Also, the value of the quantitative measurements for each denoising method on all randomly selected slices is summarized in Table 1. Furthermore, to have a comparison between time complexity of the evaluated denoising methods, the mean of the needed computation time for each slice on a PC with Microsoft Windows X32 edition, Intel core2 Duo CPU at 3.00 GHz, 4 GB RAM is reported in Table 1.

Before analyzing the results of Table 1, it should be noted that visual results of a simple Wiener filter (like those shown in Figs. 6 and 7) indicate the weakness of it in OCT image denoising, and the high value of TP and EP for the Wiener filter

in Table 1 is because of the definition of these two measures in which the similarity of the denoised image to the original one plays an important role. However, the low value of CNR for the Wiener filter emphasizes the weakness of this denoising method. Regarding the other mentioned denoising algorithms, according to Table 1, the performance of the proposed method is considerably better than the other methods in TP, which is obviously visible in Figs. 6 and 7. Performance of all of the studied methods is close to each other in EP, and the SC-GMM has the highest EP, which is obtained because of the least difference appearing in the resulting image visually. However, it cannot be considered a positive point lonely, since the values of CNR and TP for this method are very low and indeed this method does not show the proper features as a powerful method for OCT denoising. Regarding the CNR measure, the proposed method
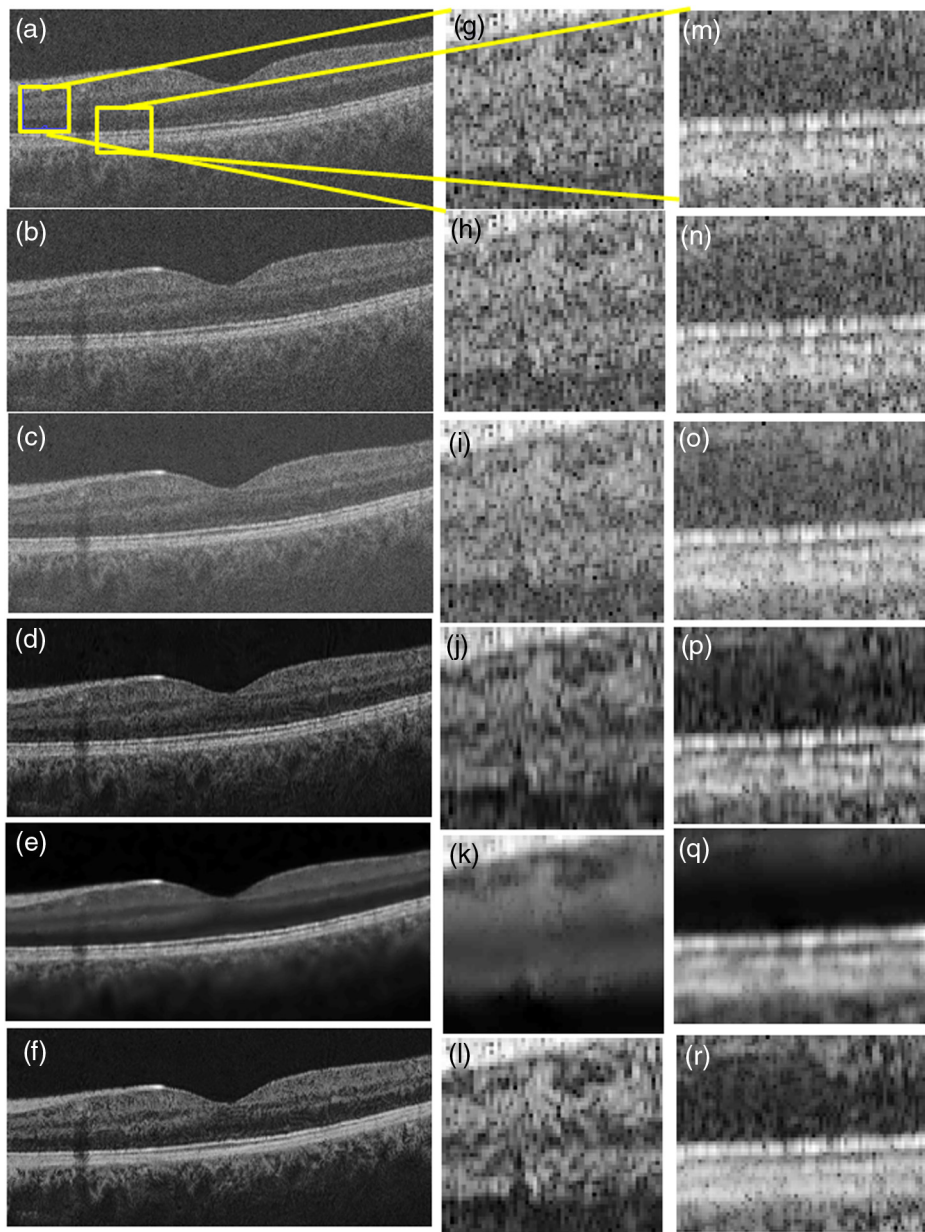

Fig. 7 Denoising results in a sample B-scan. The second and third columns show an enlargement of the specified regions of first column images. (a), (g), (m) Original noisy image; (b), (h), (n) simple Wiener; (c), (i), (o) SC-GMM; (d), (j), (p) BM3D; (e), (k), (q) 3DCWT-KSVD; and (f), (l), (r) proposed method.

and 3DCWT-KSVD have remarkably better results than others. Although 3DCWT-KSVD has the highest CNR among all studied methods, it cannot be the winner in this denoising competition because of its weak results in TP and EP; visual results in Figs. 6 and 7 also confirm this matter.

4 Discussion

The main objective of this paper is to prove the effect of Gaussianization in the result of the OCT denoising by a Wiener-based denoising method. As our results in Table 1 and Figs. 6 and 7 show, it is obviously clear that using the proposed combined method has been much more successful than the SC-GMM method, which assumes Gaussianity for the noise-free image without any justification for proposing this assumption on OCT datasets.

Our second goal in this work is to generally propose a significant method for OCT denoising. To investigate the power of the proposed method, a comparison with the 3DCWT-KSVD algorithm as a recent state of the art in this field and BM3D as a powerful denoising method was done. Visual results in Figs. 6 and 7 demonstrate better noise reduction using the proposed method while desired textural features are preserved simultaneously. Also, in Table 1, this matter is emphasized by checking the high value of TP in the proposed method compared with the 3DCWT-KSVD and BM3D algorithms. Regarding the CNR measures, 3DCWT-KSVD could provide higher CNR because of the very good speckle removing in the background area, but it does not mean that this method is better for next OCT processing because the main goal behind the OCT denoising is providing an appropriate dataset for the next OCT processing, such as layer segmentation[42] or lesions identification, while the denoised image obtained by the 3DCWT-KSVD method does not show this ability very well.

To demonstrate this superiority in our proposed method, A-scans of each denoised image were analyzed because many OCT segmentation methods perform based on gradient information from B-scans or analysis of A-scans in OCT datasets.[43] The high level of speckle noise in the original noisy OCT image does not allow features of the image to be detectable in segmentation processes; however, applying a good denoising algorithm that suppresses much of the speckle noise and preserves features of the image can provide more reliable segmentation. Figure 8 shows the ability of the proposed method to reduce the speckle noise and protect identifiable feature peaks and valleys. In fact, because of producing the clean and almost noiseless B-scan images in the proposed method [Fig. 8(f)], its A-scans obviously include a peak or valley for each layer of the retina, and the signal amplitude at the boundary layers can be greatly altered. In the other words, an important benefit of the proposed method is using contrast enhancement and denoising together. As depicted in our previous work,[35] applying GT on OCT images leads to contrast enhancement of the image and combination of GT and SC-GMM is a proper algorithm for simultaneously denoising and contrast enhancement.

Another way to evaluate the performance of the proposed method is by analyzing the intraretinal layer segmentation results. For this purpose, a diffusion map-based method introduced in Ref. 43 for OCT boundaries segmentation was used. This segmentation method was tested once on original OCT B-scans and another time on images denoised by each of the aforementioned denoising algorithms.

For each case, the error values were calculated as the difference of computed layer position by a diffusion map segmentation method and manually labeled values by an expert observer.

Tables 2 and 3 show the mean signed and unsigned border positioning errors for each boundary, which is obtained for 130 randomly selected B-scans from the Topcon dataset. The numbering of retinal surfaces in these tables is based on Fig. 8.

Based on Tables 2 and 3, the proposed method seems superior to the other mentioned algorithms in the segmentation of some boundaries (8th to 12th boundaries). However, to illustrate the statistically significant improvement of the proposed method over the other algorithms, Table 4 shows the obtained p-values. Based on Table 4, it can be seen that the 8th to 12th boundaries, which are more difficult to identify because of lack of contrast, are significantly better localized in the proposed method compared with the SC-GMM algorithm. Regarding the BM3D and 3DCWT-KSVD algorithms, this superiority is significant just for the 11th and 12th boundaries (p-value <0.05).

Furthermore, given that the ultimate goal of all the works in the medical image processing field is to help physicians determine better and more accurate diagnosis and treatment of disease, ranking mentioned denoising methods by an expert was considered another acceptable criterion for evaluating our method. Accordingly, an ophthalmologist was asked to score the denoised images by each method (raw data, denoised images by SC-GMM, 3DCWT-KSVD, and the proposed method) between one and four; the score of one to four is assigned "best," "very good," "good," and "worst," respectively. This ranking was done on all 130 randomly selected B-scans (some sample images are illustrated in Figs. 6 and 7) and the average score on all B-scans for our method was 1.2846 (for 110 slices of all 130 B-scans, the proposed method achieved score one), while this value for raw images was 1.8538, for SC-GMM was 2.8231, and for 3DCWT-KSVD was 3.9615. Based on this result, the superiority of the proposed method in clinical applications is also obvious.

Another noticeable issue is that in this research we worked on single-frame images provided by Topcon imaging system; hence the proposed method may become a useful step in OCT image processing approaches, where single frame detection is a must (where the data acquisition time or system restrictions do not allow for multiframe acquisition). However, to make

Table 1 Evaluation measure results; averaged over 130 OCT B-scans from the Topcon device.

	Measure			
Method	CNR	EP	TP	Computation time (s)
Original	4.9201	1.0000	1.0000	—
SC-GMM	7.2987	0.9895	0.5995	84.13
BM3D	13.0651	0.9826	0.7278	4.20
3DCWT-KSVD	39.7933	0.9316	0.1150	87.09[a]
Proposed method	22.9270	0.9653	0.9344	83.22
Simple Wiener	5.0566	1.0000	0.9969	0.54

[a]For 3DCWT-KSVD, computation time is a combination of training and testing time; i.e., first a dictionary has to be learned (on average 77.72 s per B-scan) and then the test image is denoised using the learned dictionary (on average 9.37 s per B-scan).
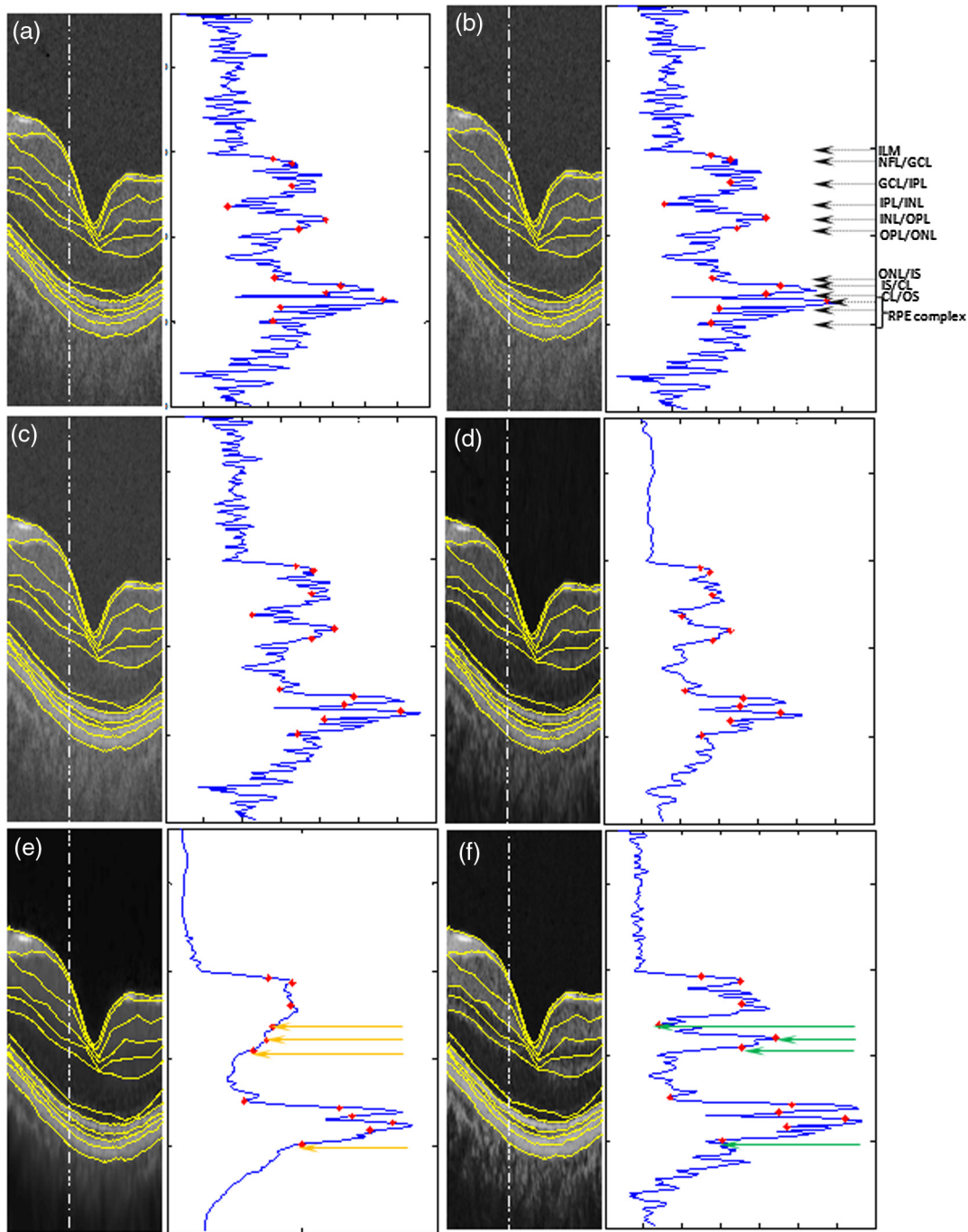
Fig. 8 The cross-section signal along the white solid line. (a) Original noisy image, (b) simple Wiener, (c) SC-GMM, (d) BM3D, (e) 3DCWT-KSVD, (f) proposed method. Red stars on the A-scans show the place of each of 12 boundaries of retinal layers. The name of these layers is ILM, internal limiting membrane; NFL, nerve fiber layer; GCL, ganglion cell layer; IPL, inner plexiform layer; INL, inner nuclear layer; OPL, outer plexiform layer; ONL, outer nuclear layer; IS, inner segment of rods and cones; CL, connecting cilia layer; OS, outer segment of rods and cones, RPE, retinal pigment epithelium, respectively, from top to down. RPE includes two surfaces and three last boundaries in our figures. Green indicators in (f) display some examples of the superiority of the proposed method in reducing the speckle noise and protecting identifiable feature peaks and valleys, compared with 3DCWT-KSVD [orange indicators in (e)].

a good judgment on the power of the method in general, it should be compared with results from a multiframe approach (as angular compounding for example), and hopefully this research can be used as a starting point for further and deeper discussions in this field in the OCT community.

5 Conclusion

In this paper, a developed denoising method for speckle reduction in OCT images was introduced. Our main issue was the effect of holding the assumptions in different statistical methods.

Table 2 Summary of mean signed border positioning errors on 12 boundaries from the Topcon dataset.

Boundary number	Original image	Simple Wiener	SC-GMM	3DCWT-KSVD	BM3D	Proposed method
1 (ILM)	0.1212	0.1302	0.1097	0.3068	0.1285	0.2237
2 (NFL/GCL)	−1.8480	−2.0569	−2.1620	−2.3537	−1.7582	−1.8392
3 (GCL/IPL)	−1.1763	−1.2456	−1.5197	−1.8303	−0.9573	−1.3748
4 (IPL/INL)	−1.1810	−1.1951	−1.8078	−3.3382	−1.3208	−2.0366
5 (INL/OPL)	1.5298	1.4110	1.1182	0.6219	1.3244	0.7859
6 (OPL/ONL)	−1.1494	−1.3285	−1.7234	−2.5095	−1.2204	−2.0787
7 (ONL/IS)	−1.7695	−1.9733	−1.7058	−1.5062	−1.9472	−1.9390
8 (IS/CL)	−0.7252	−0.7384	−0.6832	−0.5829	−0.7030	−0.5460
9 (CL/OS)	−0.8541	−0.8683	−0.8066	−0.5846	−0.8515	−0.6888
10 (RPE complex)	−0.8294	−0.8457	−0.7074	−0.3090	−0.7577	−0.6303
11 (RPE complex)	−0.7996	−0.8110	−0.7023	−0.0723	−0.7770	−0.5778
12 (RPE complex)	−0.8471	−0.8822	−0.6589	−0.6124	−0.8630	−0.1574

Table 3 Summary of mean unsigned border positioning errors on 12 boundaries from the Topcon dataset.

Boundary number	Original image	Simple Wiener	SC-GMM	3DCWT-KSVD	BM3D	Proposed method
1 (ILM)	1.2423	1.2380	1.2367	1.1956	1.1885	1.0726
2 (NFL/GCL)	2.2448	2.3854	2.3616	2.4921	2.4777	2.3974
3 (GCL/IPL)	3.1938	3.1310	3.7323	5.1035	3.3827	4.4923
4 (IPL/INL)	3.2252	3.1349	3.8814	5.7698	2.9900	4.9480
5 (INL/OPL)	3.4090	3.5000	3.7080	4.9833	3.5159	4.4966
6 (OPL/ONL)	3.3783	3.3838	3.5820	4.8286	3.1065	4.4527
7 (ONL/IS)	2.3896	2.5474	2.2852	2.0532	2.5309	2.4022
8 (IS/CL)	1.1314	1.1170	1.1273	1.0360	1.1265	0.9387
9 (CL/OS)	1.1406	1.1396	1.1362	0.9680	1.1502	0.9646
10 (RPE complex)	1.1132	1.1158	1.0441	0.9112	1.0694	0.9036
11 (RPE complex)	1.1468	1.1469	1.1785	1.3118	1.2080	1.0101
12 (RPE complex)	1.0415	1.0687	0.9615	1.0188	1.0650	0.7117

Particularly, in this work, the employed denoising algorithm (SC-GMM) was based on the Wiener filter, and in this method both noise-free data and noise are assumed to be Gaussian; however, holding this assumption has not been investigated in previous research. Since OCT datasets do not satisfy this assumption and an NLM model is fitted on these datasets, a transform to Gaussianize each component of this mixture model was needed. After constructing an image underlying GMM, SC-GMM was used for denoising. The visual and numerical results show the superiority of this combined method

and encourage us to compare the proposed method with BM3D and 3DCWT-KSVD algorithms as the state-of-the-art studies in this field. Indeed, the advantage of our method, in addition to appropriate noise reduction, is in preserving and highlighting the features of the image like textures and edges that provide a suitable dataset for the next OCT processing such as layer segmentation or object detection. This matter was demonstrated by investigating the behavior of A-scans in all mentioned denoising methods. In addition, the method was shown to improve segmentation accuracy of some intraretinal layers. Furthermore,

Table 4 Improvement of the proposed method compared with SC-GMM, BM3D, and 3DCWT-KSVD algorithm, on the 8th to 12th boundaries of retinal OCT.

Boundary number	p-value (our alg. versus SC-GMM)	p-value (our alg. versus BM3D)	p-value (our alg. versus 3DCWT-KSVD)
8 (IS/CL)	0.0044	0.0591	0.1306
9 (CL/OS)	0.0075	0.0664	0.4699
10 (RPE complex)	0.0221	0.0900	0.4441
11 (RPE complex)	0.0117	0.0457	0.0021
12 (RPE complex)	<0.0001	0.0030	0.0005

as another way to prove the superiority of the proposed method in clinical applications, the result of ranking different methods by an ophthalmologist shows predominance of the proposed method.

Disclosures

No conflicts of interest, financial or otherwise, are declared by the authors.

Acknowledgments

References

1. D. Huang et al., "Optical coherence tomography," *Science* **254**(5035), 1178–1181 (1991).
2. M. R. Hee et al., "Optical coherence tomography of the human retina," *Arch. Ophthalmol.* **113**(3), 325–332 (1995).
3. M. Pircher et al., "Speckle reduction in optical coherence tomography by frequency compounding," *J. Biomed. Opt.* **8**(3), 565–569 (2003).
4. B. F. Kennedy et al., "Speckle reduction in optical coherence tomography by strain compounding," *Opt. Lett.* **35**(14), 2445–2447 (2010).
5. Z. Amini and H. Rabbani, "Classification of medical image modeling methods: a review," *Curr. Med. Imaging Rev.* **12**(2), 130–148 (2016).
6. T. M. Jørgensen et al., "Enhancing the signal-to-noise ratio in ophthalmic optical coherence tomography by image registration—method and clinical examples," *J. Biomed. Opt.* **12**(4), 041208 (2007).
7. D. Alonso-Caneiro, S. A. Read, and M. J. Collins, "Speckle reduction in optical coherence tomography imaging by affine-motion image registration," *J. Biomed. Opt.* **16**(11), 116027 (2011).
8. D. C. Fernández et al., "Comparing total macular volume changes measured by optical coherence tomography with retinal lesion volume estimated by active contours," *Invest. Ophthalmol. Visual Sci.* **45**(13), 3072 (2004).
9. P. Puvanathasan and K. Bizheva, "Interval type-II fuzzy anisotropic diffusion algorithm for speckle noise reduction in optical coherence tomography images," *Opt. Express* **17**(2), 733–746 (2009).
10. R. Bernardes et al., "Improved adaptive complex diffusion despeckling filter," *Opt. Express* **18**(23), 24048–24059 (2010).
11. H. M. Salinas and D. C. Fernández, "Comparison of PDE-based nonlinear diffusion approaches for image enhancement and denoising in optical coherence tomography," *IEEE Trans. Med. Imaging* **26**(6), 761–771 (2007).
12. A. M. Bagci et al., "Thickness profiles of retinal layers by optical coherence tomography image segmentation," *Am. J. Ophthalmol.* **146**(5), 679–687.e1 (2008).
13. J. Rogowska and M. E. Brezinski, "Evaluation of the adaptive speckle suppression filter for coronary optical coherence tomography imaging," *IEEE Trans. Med. Imaging* **19**(12), 1261–1266 (2000).
14. A. Mishra et al., "Intra-retinal layer segmentation in optical coherence tomography images," *Opt. Express* **17**(26), 23719–23728 (2009).
15. A. R. Fuller et al., "Segmentation of three-dimensional retinal image data," *IEEE Trans. Visual Comput. Graphics* **13**(6), 1719–1726 (2007).
16. A. Wong et al., "General Bayesian estimation for speckle noise reduction in optical coherence tomography retinal imagery," *Opt. Express* **18**(8), 8338–8352 (2010).
17. F. Luan and Y. Wu, "Application of RPCA in optical coherence tomography for speckle noise reduction," *Laser Phys. Lett.* **10**(3), 035603 (2013).
18. L. Fang et al., "Sparsity based denoising of spectral domain optical coherence tomography images," *Biomed. Opt. Express* **3**(5), 927–942 (2012).
19. L. Fang et al., "Fast acquisition and reconstruction of optical coherence tomography images via sparse representation," *IEEE Trans. Med. Imaging* **32**(11), 2034–2049 (2013).
20. D. C. Adler, T. H. Ko, and J. G. Fujimoto, "Speckle reduction in optical coherence tomography images by use of a spatially adaptive wavelet filter," *Opt. Lett.* **29**(24), 2878–2880 (2004).
21. V. Gupta et al., "Computerized automation of wavelet based denoising method to reduce speckle noise in OCT images," in *Int. Conf. on Information Technology and Applications in Biomedicine (ITAB 2008)*, IEEE (2008).
22. M. A. Mayer et al., "Wavelet denoising of multiframe optical coherence tomography data," *Biomed. Opt. Express* **3**(3), 572–589 (2012).
23. H. Rabbani, M. Sonka, and M. D. Abramoff, "Optical coherence tomography noise reduction using anisotropic local bivariate Gaussian mixture prior in 3D complex wavelet domain," *J. Biomed. Imaging* **2013**, 417491 (2013).
24. Z. Jian et al., "Speckle attenuation in optical coherence tomography by curvelet shrinkage," *Opt. Lett.* **34**(10), 1516–1518 (2009).
25. Z. Jian et al., "Three-dimensional speckle suppression in optical coherence tomography based on the curvelet transform," *Opt. Express* **18**(2), 1024–1032 (2010).
26. R. Kafieh et al., "Curvature correction of retinal OCTs using graph-based geometry detection," *Phys. Med. Biol.* **58**(9), 2925–2938 (2013).
27. R. Kafieh, H. Rabbani, and I. Selesnick, "Three dimensional data-driven multi scale atomic representation of optical coherence tomography," *IEEE Trans. Med. Imaging* **34**(5), 1042–1062 (2015).
28. N. M. Grzywacz et al., "Statistics of optical coherence tomography data from human retina," *IEEE Trans. Med. Imaging* **29**(6), 1224–1237 (2010).
29. A. Buades, B. Coll, and J.-M. Morel, "A non-local algorithm for image denoising," in *IEEE Computer Society Conf. on Computer Vision and Pattern Recognition (CVPR 2005)*, IEEE (2005).
30. M. Elad and M. Aharon, "Image denoising via sparse and redundant representations over learned dictionaries," *IEEE Trans. Image Process.* **15**(12), 3736–3745 (2006).
31. K. Dabov et al., "Image denoising by sparse 3-D transform-domain collaborative filtering," *IEEE Trans. Image Process.* **16**(8), 2080–2095 (2007).
32. M. Niknejad, H. Rabbani, and M. Babaie-Zadeh, "Image restoration using Gaussian mixture models with spatially constrained patch clustering," *IEEE Trans. Image Process.* **24**(11), 3624–3636 (2015).
33. X. Li, "Exemplar-based EM-like image denoising via manifold reconstruction," in *17th IEEE Int. Conf. on Image Processing (ICIP 2010)*, IEEE (2010).
34. G. Yu, G. Sapiro, and S. Mallat, "Solving inverse problems with piecewise linear estimators: from Gaussian mixture models to structured sparsity," *IEEE Trans. Image Process.* **21**(5), 2481–2499 (2012).
35. Z. Amini and H. Rabbani, "Statistical modeling of retinal optical coherent tomography," *IEEE Trans. Med. Imaging* **35**(6), 1544 (2016).
36. A. P. Dempster, N. M. Laird, and D. B. Rubin, "Maximum likelihood from incomplete data via the EM algorithm," *J. Royal Stat. Soc. Ser. B (Methodol.)* **39**(1), 1–38 (1977).

37. H. Rabbani et al., "Speckle noise reduction of medical ultrasound images in complex wavelet domain using mixture priors," *IEEE Trans. Biomed. Eng.* **55**(9), 2152–2160 (2008).
38. H. Rabbani, M. Vafadust, and S. Gazor, "Image denoising based on a mixture of Laplace distributions with local parameters in complex wavelet domain," in *IEEE Int. Conf. on Image Processing*, IEEE (2006).
39. H. Rabbani, R. Nezafat, and S. Gazor, "Wavelet-domain medical image denoising using bivariate Laplacian mixture model," *IEEE Trans. Biomed. Eng.* **56**(12), 2826–2837 (2009).
40. A. Pizurica et al., "Multiresolution denoising for optical coherence tomography: a review and evaluation," *Curr. Med. Imaging Rev.* **4**(4), 270–284 (2008).
41. Q. Yang et al., "Automated layer segmentation of macular OCT images using dual-scale gradient information," *Opt. Express* **18**(20), 21293–21307 (2010).
42. L. Fang et al., "Segmentation based sparse reconstruction of optical coherence tomography images," *IEEE Trans. Med. Imaging* **36**(2), 407–421 (2016).
43. R. Kafieh et al., "Intra-retinal layer segmentation of 3D optical coherence tomography using coarse grained diffusion map," *Med. Image Anal.* **17**(8), 907–928 (2013).

Zahra Amini received her BSc degree from Isfahan University of Technology (IUT), Iran, in 2007, her MSc degree from the University of Yazd, Iran, in 2011, both in electrical engineering (communications), and her PhD in biomedical engineering from Isfahan University of Medical Sciences, Iran, in 2016. She is currently an assistant professor in the Department of Biomedical Engineering, School of Advanced Technologies in Medicine, Isfahan University of Medical Sciences. Her research interests include medical image modeling, signal and image processing, sparse transforms, and brain computer interface.

Hossein Rabbani received his BSc degree in electrical engineering from Isfahan University of Technology in 2000 with the highest honors, and his MSc degree and PhD in bioelectrical engineering in 2002 and 2008, respectively, from Tehran Polytechnic. In 2007, he was at Queen's University, as a visiting researcher; in 2011 at University of Iowa as a postdoctoral research scholar; and from 2013 to 2014 at Duke University Eye Center as a postdoctoral fellow. He is now senior member of IEEE and an associate professor in Biomedical Engineering Department and MISP Research Center, Isfahan University of Medical Sciences. His main research interests are medical image analysis and modeling, sparse transforms, and image restoration. He has published more than 110 papers as an author or coauthor in these areas.